Article
Vol. 26, No. 1, p. 95–112, February 2022
https://doi.org/10.1007/s12303-021-0014-6
pISSN 1226-4806 eISSN 1598-7477
Geosciences Journal GJ

Deep electrical structure and dynamic mechanism of the Yinchuan Graben on the western margin of the Ordos Block

Gang Min[1]*, Bingxi Yin[2], Jinchao Chen[1], Yong Yang[2], Huiling Yuan[1], and Yan Wang[1]

[1]Key Laboratory of Earth Exploration and Information Technology of the Ministry of Education, Chengdu University of Technology, Chengdu 610059, China
[2]Ningxia Bureau of Geology and Mineral Exploration and Development, Yinchuan 750021, China

ABSTRACT: The Yinchuan Graben (YG) is situated in the transitional area between the Tibetan Plateau, Ordos Block (OB) and Alxa Block (AB). The dynamic mechanism of the YG is controversial because of its unique tectonic environment. This study used a broadband magnetotelluric profile constrained by high-density point spacing to reliably obtain the deep electrical structure across the Helanshan Orogenic Belt and YG and to discuss the dynamic mechanism of the YG. The main research results are as follows. 1) Our profile and previous seismic profiles show a low-resistivity and low-velocity body in the deep YG, which extends upward and cuts through the bottom boundary of the upper crust, and all results indicate that this body may be the result of partial melting due to upwelling mantle material. 2) Our profile also shows a high-resistivity anomaly in the middle–lower crust of the Helanshan orogenic belt, which can be interpreted as intrusive rocks formed by the emplacement of partially melted materials. 3) The Helanshan east piedmont fault dips eastward and intersects with the Yellow River fault at the depth of 20 km, and the typical structure of the intersection may be the seismogenic structure of the Pingluo Ms8.0 earthquake. 4) The evolution of the YG may have been controlled by various dynamic mechanisms, and the initial formation of the YG may have resulted from the upwelling mantle material beneath the northern OB; the evolution of the YG since 10 Ma may also have been affected by lateral mantle flow from the Tibetan Plateau to the gap between the OB and AB.

Key words: Yinchuan Graben, Helanshan orogenic belt, electrical structure, Ordos Block, Tibetan Plateau, tectonic evolution

Manuscript received June 5, 2020; Manuscript accepted March 9, 2021

1. INTRODUCTION

The basin-and-range structure composing the Yinchuan Graben (YG) and the Helanshan Orogenic Belt (HOB) is situated on the border of three active blocks: the northeast Tibetan Plateau, Alxa Block and Ordos Block (Zhang et al., 2003). The study area forms the northern segment of the North-South Seismic Belt in the Chinese mainland, which is characterized by high seismicity and a high risk of strong earthquakes (Shao and Zhang, 2013; Wang et al., 2015). Previous studies have indicated that the destruction of the North China Craton (NCC) since the Mesozoic occurred mainly in eastern China, while the central-western section of the NCC remains stable and has undergone only partial lithospheric thinning and reconstruction (Wu et al., 1988; Menzies et al., 1993; Griffin et al., 1998; Zheng et al., 2001). However, the OB, situated in the central-western section of the NCC, has experienced intense tectonic movements since the Cenozoic, and many rift systems have formed around this block, including the YG (Deng et al., 1999; Li et al., 2010; Zhao et al., 2012). In view of the complex tectonic setting, the structural movements caused by the destruction of the NCC and the NE-trending expansion of the northeastern Tibetan Plateau may both be related to the evolution of the YG; therefore, researching the characteristics of crust-mantle structure in the YG and adjacent areas is of great scientific value. Moreover, the occurrence of earthquakes is closely related to the structure of the crust and upper mantle, physical properties of the medium and deep

*Corresponding author:
Gang Min
Key Laboratory of Earth Exploration and Information Technology of the Ministry of Education, Chengdu University of Technology, No. 1, Erxianqiao Dongsan Road, Chenghua District, Chengdu 610059, China
Tel: +86-15928002361, E-mail: mg-s1983827@163.com

dynamic environment (Xu et al., 2014). Thus, researching the deep structure is important for understanding the structural mechanism of moderate to strong earthquakes.

Many petroleum seismic exploration profiles were introduced in the book "Active Fault Detection and Earthquake Risk Assessment in Yinchuan City" (Chai et al., 2011), but because their exploration depth is limited, these petroleum seismic profiles can only be used to analyse the characteristics of upper crustal tectonic deformation. In recent years, research on the deep seismic sounding profiles and natural earthquake data has allowed the crust to upper mantle structure of the YG and adjacent regions to be reconstructed, which clearly reveals the tectonic deformation characteristics of the study area (Tian et al., 2011; Jiang et al., 2013; Liu et al., 2017; Shen et al., 2017; Wang et al., 2017; Gao et al., 2018; Guo et al., 2018; Wang et al., 2018). These findings from previous seismic studies provide references for the comprehensive research reported in this paper.

The magnetotelluric (MT) method is one of the main geophysical methods for investigating the electrical structure of the Earth's crust and mantle and plays an important role in studies of the deep structure of active faults and seismogenic structures (Becken et al., 2011; Zhao et al., 2014; Mohan et al., 2015), the distribution of highly conductive layers in the crust to upper mantle (Wei et al., 2001; Wannamaker et al., 2002; Bai et al., 2010), and the crustal and lithospheric structure (Wang et al., 2014; Murphy and Egbert, 2017), which is crucial for research on continental dynamics. MT results across the YG and adjacent areas (Qu et al., 1998; Wang et al., 2010; Dong et al., 2014; Xu et al., 2017) have also revealed the crustal and lithospheric structure of the crust and upper mantle. However, compared to the detailed velocity structures revealed by seismic studies, the electrical structure of the YG and adjacent regions has not been well studied, and the deep electrical structure in the middle section of YG is particularly unclear. These limitations have hindered the systematic understanding of the deep electrical structure and tectonic deformation of the YG.

Previous geophysical studies conducted on the YG and adjacent areas were mostly limited to a single method or small region (Wang et al., 2010; Chai et al., 2011; Feng et al., 2011; Liu et al., 2017); therefore, it has been difficult to gain a comprehensive understanding of the dynamic mechanism of the YG and the seismogenic mechanism of the Pingluo Ms8.0 earthquake (in the YG). In this paper, we use the broadband MT (BBMT) profile across the middle section of the YG, considering the previous results from seismic and MT data, and analyse and discuss the structural characteristics of the YG and adjacent regions, including the relations of adjacent blocks, the dynamic background of the YG, and the seismogenic structure of the Pingluo earthquake.

2. TECTONIC SETTING AND MAGNETOTELLURIC PROFILE

Our study area is the YG and adjacent areas, surrounded by the Ordos Block (OB), the Alxa Block (AB) and the northeastern margin of the Tibetan Plateau (Fig. 1). The OB is a relic of the NCC that exhibits little seismicity and has been tectonically stable throughout the Cenozoic (Zhang et al., 1998). The AB is part of the old Asian lithosphere (Song et al., 2006). The northeastern margin of the Tibetan Plateau (NEMTP) is a frontier area where the Tibetan Plateau is expanding northeastward, and the YG is part of the Circum-Ordos rifting systems initiated in the past few million years (Zhang et al., 1998).

The YG is an enclosed, low-lying structure with a length of 160 km and a width of 50–55 km that formed because of the extensional and shearing tectonic environment during the Cenozoic (Chai et al., 2011). The YG and HOB form part of a typical basin-and-range system on the northwestern margin of the OB (NWMOB); the evolution of the YG is controlled by the normal boundary faults: the Helanshan east piedmont fault (HEPF) to the west and the Yellow River fault (YRF) to the east (Liu etal., 2010); the southern boundary fault of the YG is the Shanguankou fault (SGKF); and the Luhuatai fault (LF) and Yinchuan fault (YF) are present in the YG (Fang et al., 2009).

As shown in Figure 1, the BBMT profile used to reconstruct the 2D electrical conductivity structure of the YG and adjacent areas is located in the middle section of the YG. From west to east, the profile spans the Jartai-Bayanhaote Graben (JT-BYG), the southeastern margin of the AB, the HOB, the YG, and the NWMOB. This profile is approximately 139 km long, with station intervals of approximately 2–5 km, and a total of 57 BBMT stations were deployed and completed.

3. DATA ACQUISITION, PROCESSING AND ANALYSIS

3.1. Data Acquisition and Processing

The data were acquired using commercial MT instruments made in Canada, namely, MTU-5A. The electric and magnetic field time series were measured parallel and perpendicular to geomagnetic north. In addition, we collected BBMT data by ensuring that the recording time of every BBMT station exceeded 24 h and by measuring the BBMT stations repeatedly in areas of higher cultural noise; further, the time series were recorded using a remote reference technique (Gamble et al., 1979) to reduce the bias from incoherent noise. The time series were processed using a statistically robust algorithm (Egbert and Booker, 1986) to compute MT transfer functions in a period range of ~320 Hz

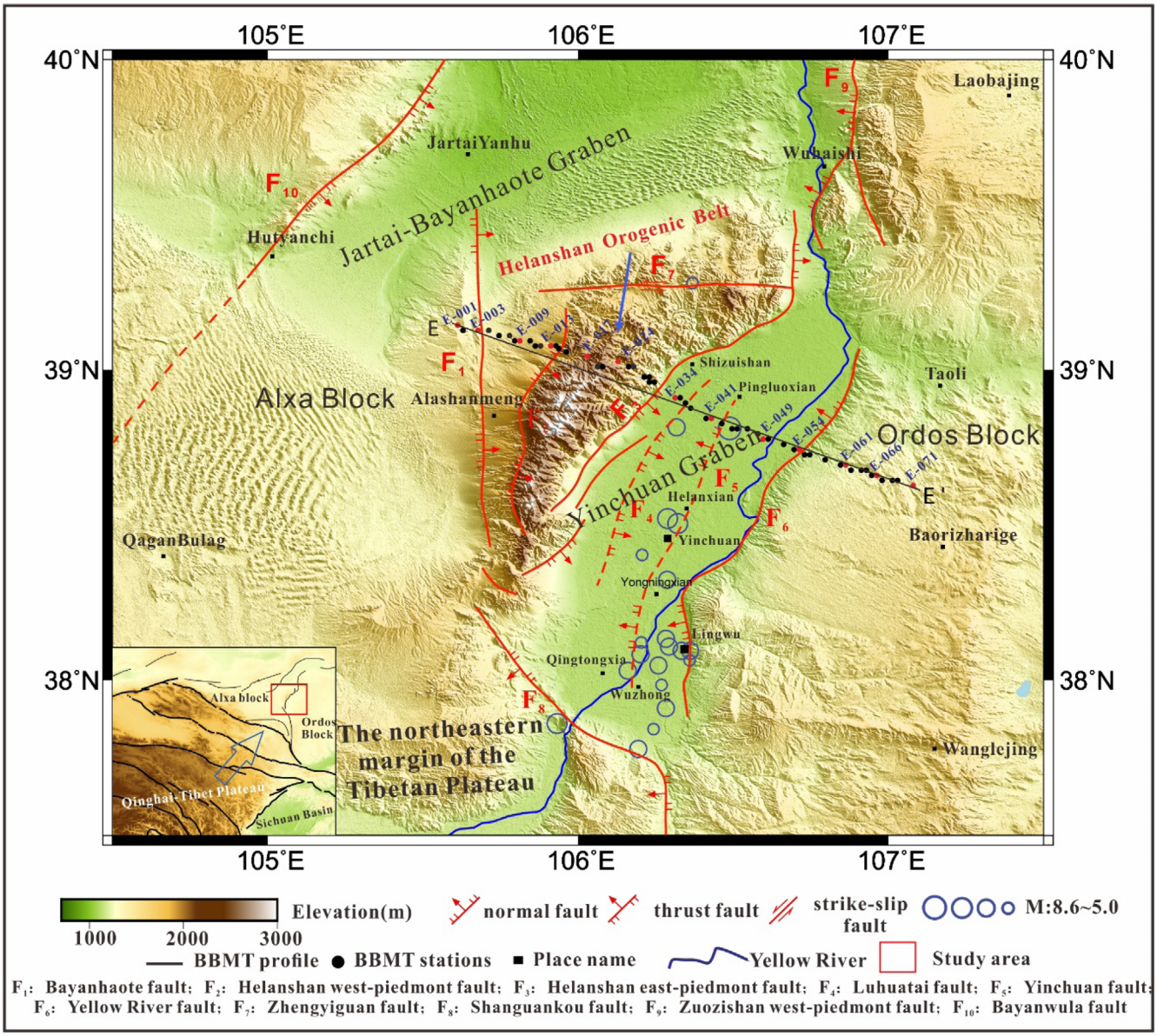

Fig. 1. Topographic map showing the major tectonic structures of the survey area and locations of the BBMT stations (black dots). The blue circles are epicenters of earthquakes (M ≥ 5.0). The red box in the inset map shows the location of the study area with respect to the northeastern margin of the Tibetan Plateau.

to ~2000 s, and the apparent resistivity and impedance phase could then be obtained. The BBMT data were generally of excellent quality because of the advanced data acquisition and processing technology that we used.

3.2. Data Analysis

Whether a 2D or 3D inversion and interpretation approach is more appropriate can be determined by the geotectonic dimensionality (Cai et al., 2010). In addition, the results of structural strike analysis are very important for the choice of data polarization mode in MT 2D inversion. The skewness and best electrical spindle azimuth are sensitive to geotectonic dimensionality and structural strike. Considering the advantages of avoiding the effect of galvanic electric field and not assuming prior dimensionality, we used the phase tensor decomposition technique (Caldwell et al., 2004) to evaluate the dimensionality and electrical spindle azimuth of our data.

The coloured section map (Fig. 2) shows the phase tensor skew angle β and denotes dimensionality at different periods of the BBMT response. The β values indicate the three dimensionality of the regional electrical structure (Caldwell et al., 2004). The β values in the frequency range of 320–0.001 Hz are small in the AB, which indicates a mostly simple structure related to weak

https://doi.org/10.1007/s12303-021-0014-6

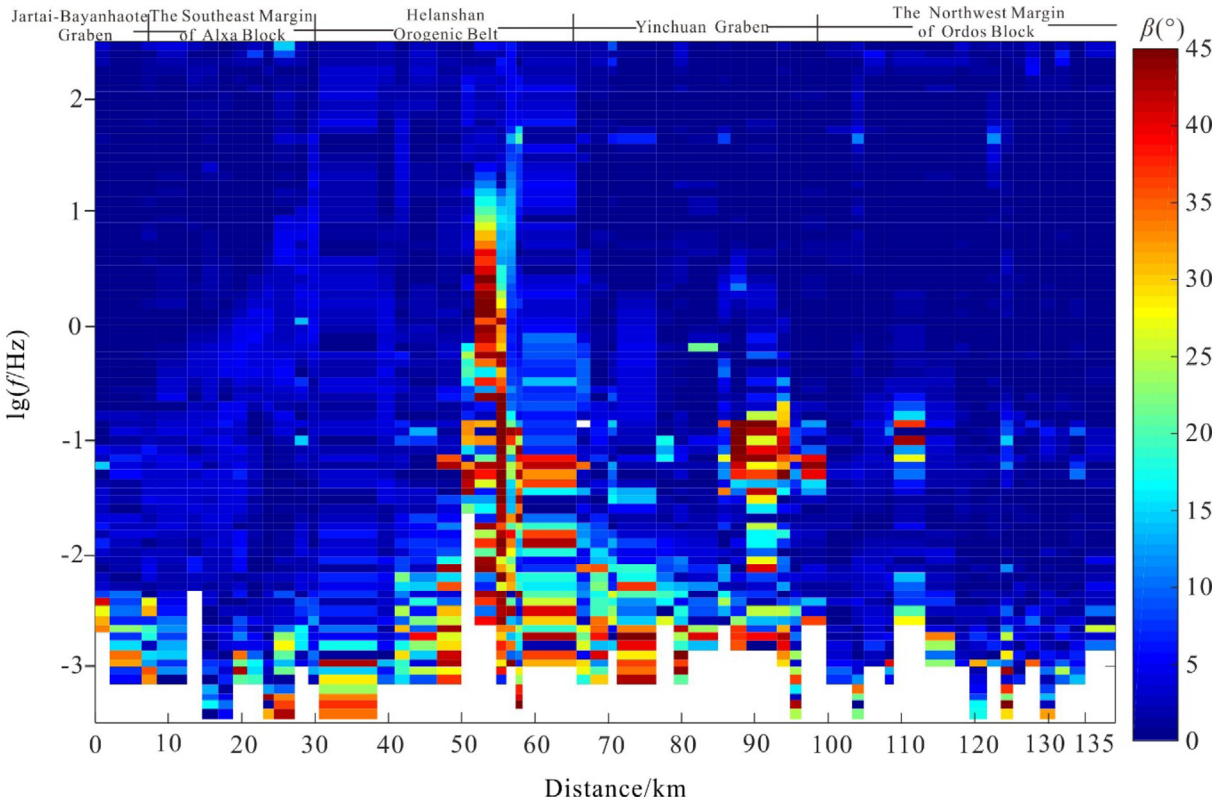

Fig. 2. The skewness using the phase tensor decomposition technique along profile E–E′. The small β indicates that one of the principal axes of the phase tensor is oriented close to the regional strike direction in 2-D and 3-D cases (Caldwell et al., 2004; Xiao et al., 2013).

tectonic deformation. The β values in the HOB and YG are complex; the values in shallow structures are small, and the values increase as the frequency decreases, indicating strong tectonic deformation or increasing noise levels, and only the structures in the deep parts of these areas cannot be treated as 2D structures. The β values in the frequency range of 320–0.001 Hz are small in the OB, which indicates a simple structure consistent with the thick and stable sediments in the OB. Based on the above analysis, the β values indicate that the geo-electrical structure can be treated as a 2D structure, in general; thus, 2D interpretation methods can be used for our profile.

The rose diagrams (Fig. 3) show the best geo-electrical spindle

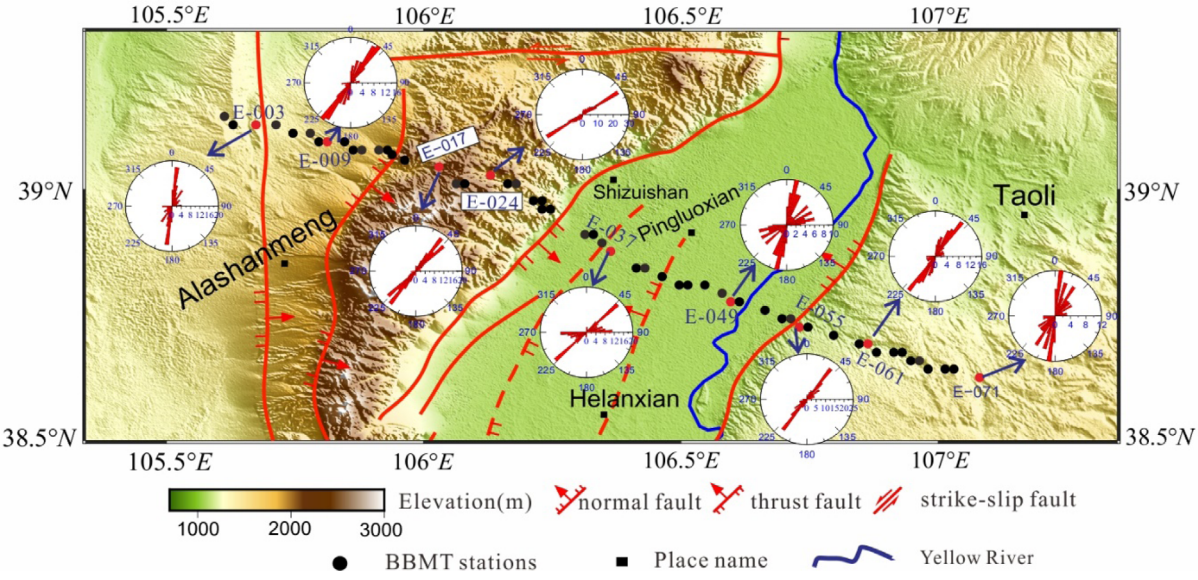

Fig. 3. Rose diagrams of the best geo-electrical spindle azimuths in different structures from phase tensor decomposition.

azimuths using the phase tensor decomposition technique. The orientations of phase tensor spindles indicate the dominant flow direction of induced currents and reflect lateral resistivity variations in the subsurface structures (Caldwell et al., 2004; Dong et al., 2014). The directions shown by the phase tensor rose diagrams for BBMT stations in different tectonic belts are generally consistent with the strike direction of the boundary faults, except that the rose diagram for station E-071 from the OB displays a dominant coherent N-S direction. As we know, MT data can be separated into transverse electric (TE) mode and transverse magnetic (TM) mode, which correspond to electrical currents flowing along and across strike, respectively (Chave and Jones, 2012) in 2D interpretations of MT. Because the BBMT data are measured parallel and perpendicular to geomagnetic north, we rotated all BBMT data to ensure that geomagnetic north is generally consistent with geo-electrical spindle azimuths. As a result, the data that are mainly parallel to the geo-electrical spindle are in TE mode, while the data perpendicular to the geo-electrical spindle are in TM mode.

3.3. The Response Curves of Typical Stations

The frequency range of the final BBMT data is ~320 Hz to ~2000 s. Figure 4 shows the sounding curves with error bar of some typical BBMT stations.

Site E-003 is situated in the JT-BYG, and the curves of the TE

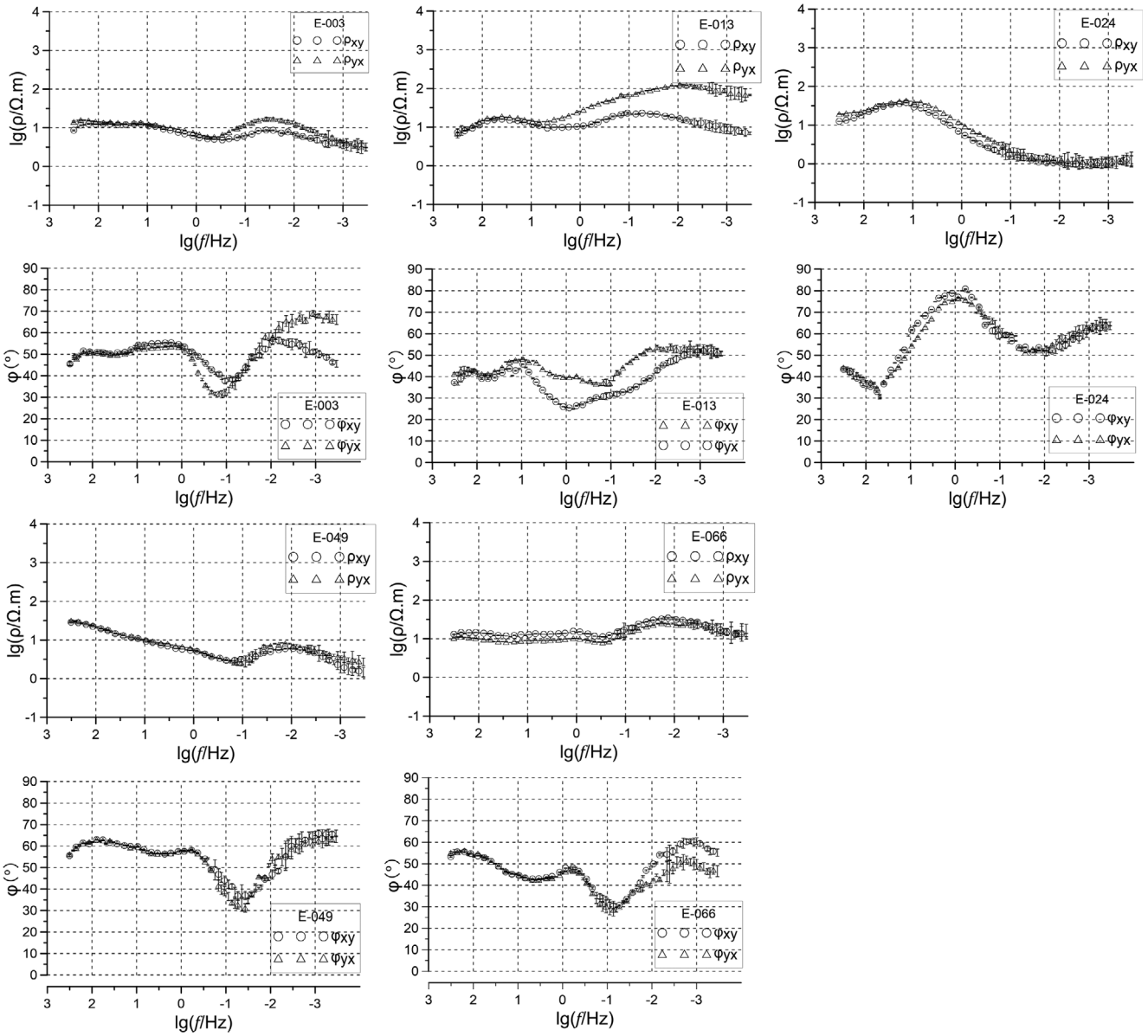

Fig. 4. The apparent resistivity and impedance phase curves with error bar for typical stations along our profile. The upper panels show the resistivity curves, and the lower panels show the impedance phase curves. The error bars for the observed data are the modified error floors used in the inversion. The locations of the stations are shown in Figure 1.

https://doi.org/10.1007/s12303-021-0014-6

and TM modes both show the variation characteristics of decrease-increase-decrease from high frequency to low frequency. The values of apparent resistivity in the frequency range from ~320 Hz to ~1 Hz are relatively low and less than 32 Ω·m, which may be caused by the shallow sediments. The values of apparent resistivity in the frequency range from ~1 Hz to ~0.05 Hz show an uptrend, which means that high-resistivity structures exist beneath the sediments and may represent the basement structure. Finally, the values of apparent resistivity in the frequency range of ~0.05 Hz to 0.001 Hz show a downtrend, which indicates that low-resistivity structures exist beneath the basement.

Site E-013 is situated on the southeastern margin of the AB, and curves in the frequency range from ~320 Hz to ~1 Hz in TE and TM modes show nearly the same values, the lower apparent resistivity of which may be caused by the shallow sediments. In the frequency range from ~0.1 Hz to ~0.001 Hz, the apparent resistivity of the two modes show different values and variation trends, which indicate prominent non-2D features. The curves of both modes in the periods range ~10 s to ~2000 s increase at first and then decrease, which indicates that higher resistivity in the Palaeozoic strata and underlying lower resistivity bodies are developed beneath the Palaeozoic strata (Wang et al., 2010; Huang et al., 2013).

Site E-024 is located in the HOB, where the curves of two modes have the same variation trend, which indicates that the deep structure has obvious stratification characteristics. In the frequency range from ~320 Hz to ~10 Hz, the apparent resistivities show upward trends, which indicate that the shallow structures are characterized by high resistivity. In the frequency range from ~10 Hz to ~0.01 Hz, the apparent resistivities decrease sharply, and we infer a low-resistivity anomaly beneath the high-resistivity layers. Finally, in the frequency range from ~0.01 Hz to ~0.001 Hz, the apparent resistivities show upward trends with relatively small gradients, which indicates that the layers under the low-resistivity anomaly are characterized by high resistivity.

Site E-049 is located in the YG, and the curves of the two different modes have the same variation trend of decrease-increase-decrease. The values of the two curves are basically the same. In the frequency range from ~320 Hz to ~0.1 Hz, the apparent resistivities show downward trends, which indicate that the shallow Quaternary sediments beneath the YG are characterized by low-resistivity anomalies. In the frequency range from ~0.1 Hz to ~0.01 Hz, the apparent resistivities show upward trends, which indicate that high resistivity has developed under the sediments, which may represent the basement. The apparent resistivities show a slow downward trend in the frequency range from ~0.01 Hz to ~0.001 Hz, which indicates that the formations under the basement are characterized by low resistivity.

Site E-066 is situated in the NWMOB, and the curves of two different modes have the same variation trends and nearly the same values, which indicate that the electrical structure shows layered characteristics. In the frequency range from ~320 Hz to ~0.5 Hz, the apparent resistivity amplitudes vary approximately 10 Ω·m, which may be caused by the shallow sediments. In the frequency range from ~0.50 Hz to ~0.01 Hz, the curves show upward trends, which indicate that the units under the sediments are characterized by high resistivity. In the frequency range from ~0.01 Hz to ~0.001 Hz, the apparent resistivities show slow downward trends, which indicate a low-resistivity anomaly under the high-resistivity bodies.

4. 2D INVERSION AND DEEP ELECTRICAL STRUCTURE

4.1. The Quality of MT Data Presentation and MT Analysis

A synthetic test of the MT data considering the synthetic noise is very important since the inclusion of noise can dramatically change the resolution of MT methods. In fact, the error bar shown in MT sounding curves can reflect the noise level of MT observation data. Because it is difficult to estimate the measured

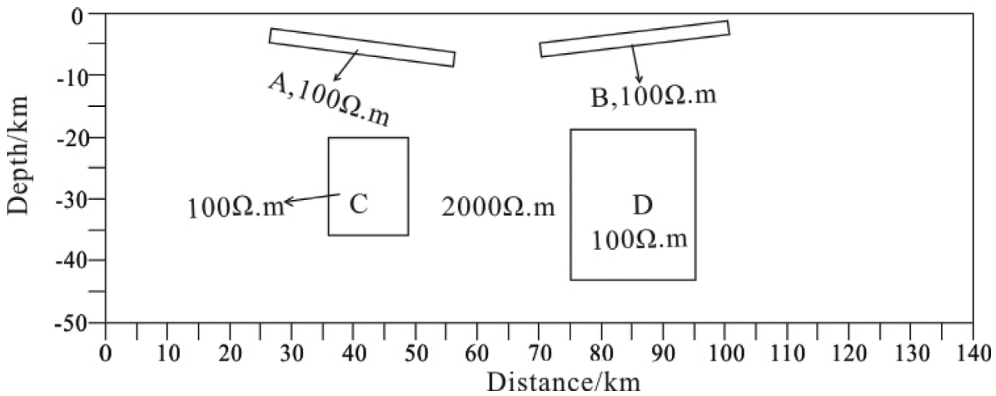

Fig. 5. The geo-electrical model embedded conductive bodies. The black boxes show the range of conductive bodies named A, B, C and D.

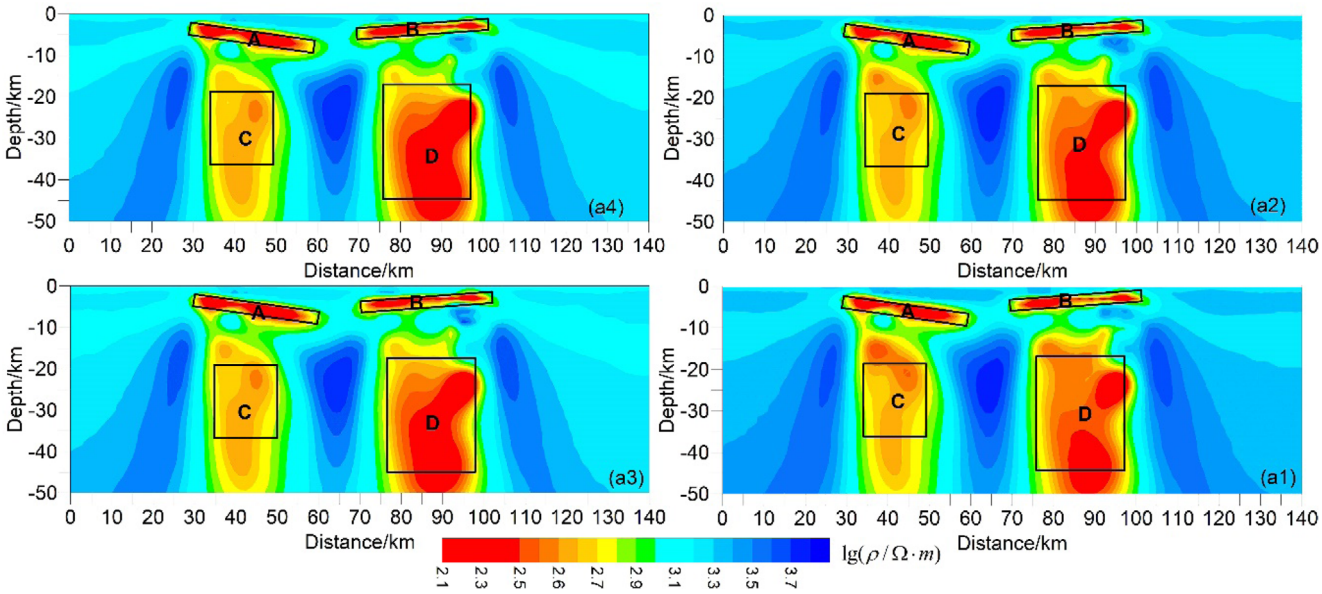

Fig. 6. The inversion results of forward synthetic data with different noise levels. (a1) The inversion result of synthetic data with no random noise; (a2) The inversion result of synthetic data with 5% random noise; (a3) The inversion result of synthetic data with 10% random noise; (a4) The inversion result of synthetic data with 12% random noise. The black boxes show the range of conductive bodies shown in Figure 5.

noise level, so generally only the error range can be estimated. We estimate the noise level of the original data is about 2–12% based on the error bar shown in sounding curves.

According to the distribution characteristics of anomalies in the study area, a typical geo-electric model is established, as shown in Figure 5, low-resistivity bodies named A, B, C and D are developed in deferent parts of the geo-electric model, and the resistivity values of these conductive bodies are 100 Ω· m.

Base on the forward data of geo-electric model, we have created synthetic data with different noise levels and then perform the synthetic inversions. The finite element method (FEM) (Jin et al., 1988) was used to carry out forward simulation. After forward simulation, we created synthetic data with deferent noise levels, and the nonlinear conjugate gradient (NLCG) algorithm (Rodi and Mackie, 2001) was used to carry out 2D inversion and interpretation, the inversion results are shown in Figure 6.

As shown in Figure 6, the inversion results of forward synthetic data with different noise levels are basically consistent, which can better reflect the spatial distribution of low resistivity anomalies. The above tests show that the inclusion of the synthetic noise can not change the resolution of MT methods.

4.2. Static Shift Correction and 2D Inversion

The electrical structure of the shallow surface along our profile is generally complex and shows obvious lateral inhomogeneity near some stations; therefore, we need to analyse the static shift phenomena of all BBMT data before 2D inversion. First, for BBMT stations in the same strata unit, we performed statistical analysis and comparison of apparent resistivity in the high-frequency band. Then, considering the physical properties of the strata, we selected data with static shifts and corrected them. In addition, static shift coefficients were recurrently adjusted in the process of inversion according to the fitting degree between measured values and calculated values from the 2D theoretical response.

In this paper, BBMT data processing and inversion calculations of our profile were carried out on the WinGlink software platform developed by the Geosystem Corporation of Italy. The stations were mainly deployed along the direction perpendicular to tectonic strike, and the data could be sensitive to near-surface 3D effects (Ledo et al., 2002; Unsworth et al., 2004). In addition, the data in TM mode would be the preferred choice for 2D inversion of field data, as suggested by forward studies (Cai and Chen, 2010). The data in TM mode were inverted with the 2D nonlinear conjugate gradient (NLCG) algorithm (Rodi and Mackie, 2001), and we constructed a 100 Ω·m half-space for the starting model. We inverted the TM and TE data together and individually and investigated the range of error floor and roughness regularization parameter (τ). Figure 7 shows the trade-off results between the model roughness and root-mean-square (RMS) misfits. The optimal model was chosen when τ is 10, and the error floors were set to 10% and 1.65° (equivalent to 5% in resistivity) for TM apparent resistivity and impedance, respectively.

Figure 8 shows a comparison between the observed data and the 2D theoretical response data, and we can see that the apparent

https://doi.org/10.1007/s12303-021-0014-6

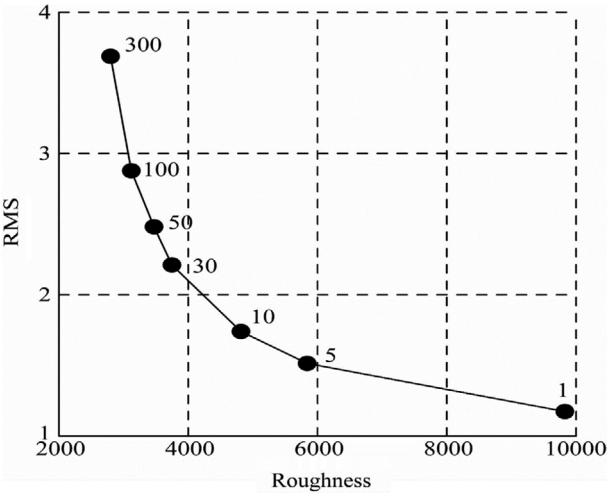

Fig. 7. L-curve of RMS values and roughness for TM data at MT stations in a range of τ. The numbers to the right of the black circle show the value of τ.

resistivity and impedance phase of the TM mode are generally well fit along our profile, which indicates that the geo-electrical model derived by inverting TM data is correct and can be used to analyse the deep electrical structure characteristics of the YG and adjacent areas.

4.3. Characteristic of Main Faults

Figure 9 shows the interpretation of fault systems and secondary structures based on the previous results from geological (Zhang et al., 2006; Liu et al., 2010; Chai et al., 2011), MT (Wang et al., 2010) and seismic sounding studies (Zhao et al., 2009; Lin et al., 2017; Liu et al., 2017; Wang et al., 2018). The resistivity model displays great lateral inhomogeneity, and the main boundary fault zones correspond to resistivity gradient zones in the 2D inversional geo-electrical model.

The F_1 and F_2 faults are located on the western side of the HOB, and the interpretation of deep seismic reflection results have shown that F_1 and F_2 are east-dipping listric thrust faults (Wang et al., 2018). In our profile, F_1 is a boundary fault between JT-BYG and the southeast AB; R1 and R2 are located on the left and right sides of the F_1 fault, respectively. Based on the spatial position relationship of R1 and R2, as well as the shape of the resistivity gradient zone between them, F_1 is inferred to be an eastward-dipping thrust fault, while F_2 is a boundary fault between the AB and the HOB and is a thrust fault with a strike-slip component (Lei et al., 2016, 2017). The gradient zone between R2 and R7 may be caused by the fracture zone of F_2, which is

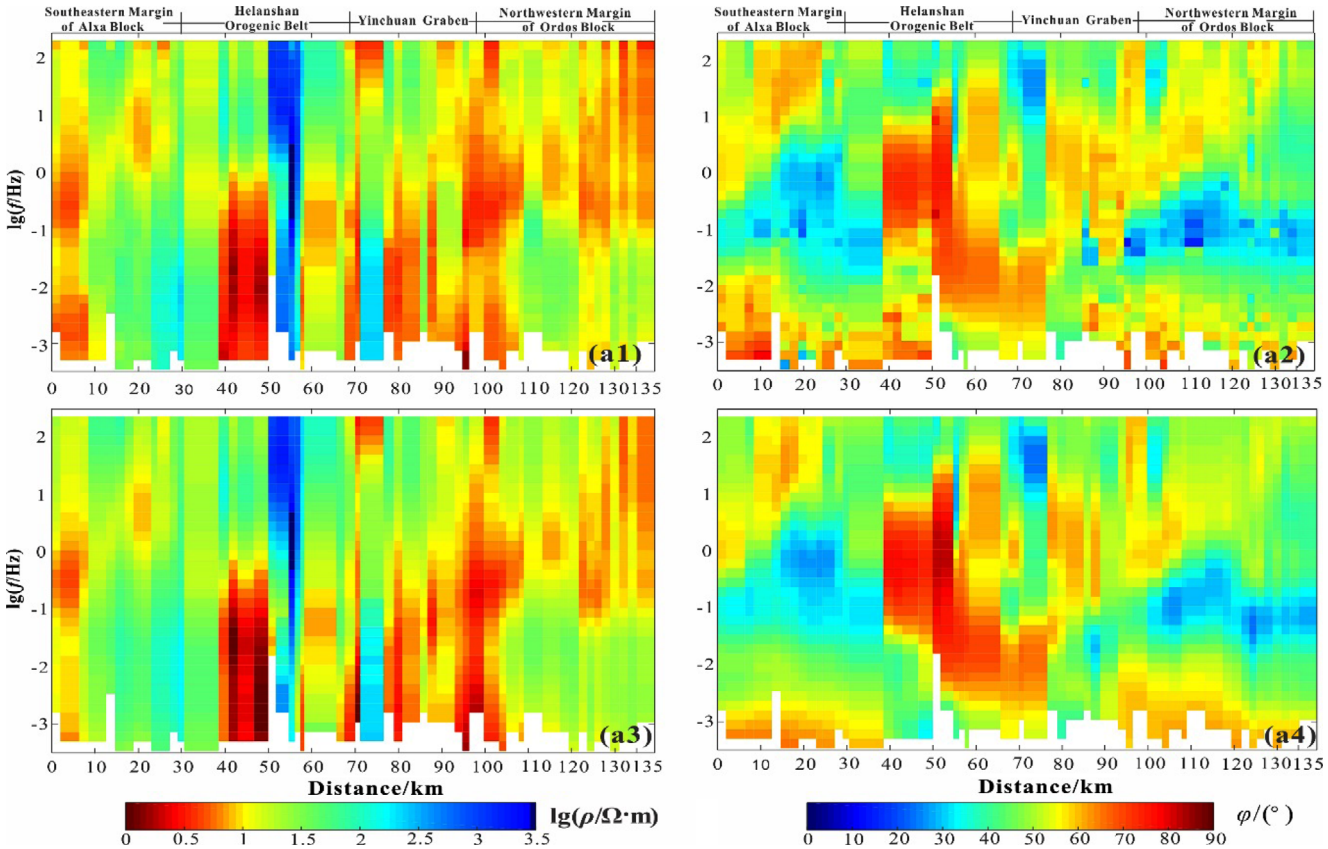

Fig. 8. Comparison of TM apparent resistivity and impedance phase with measured values and calculated values from 2D theoretical response along profile E–E′. (a1) The apparent resistivity of measured values; (a2) The impedance phase of measured values; (a3) The apparent resistivity of calculated values from 2D theoretical response; (a4) The impedance phase of calculated values from 2D theoretical response.

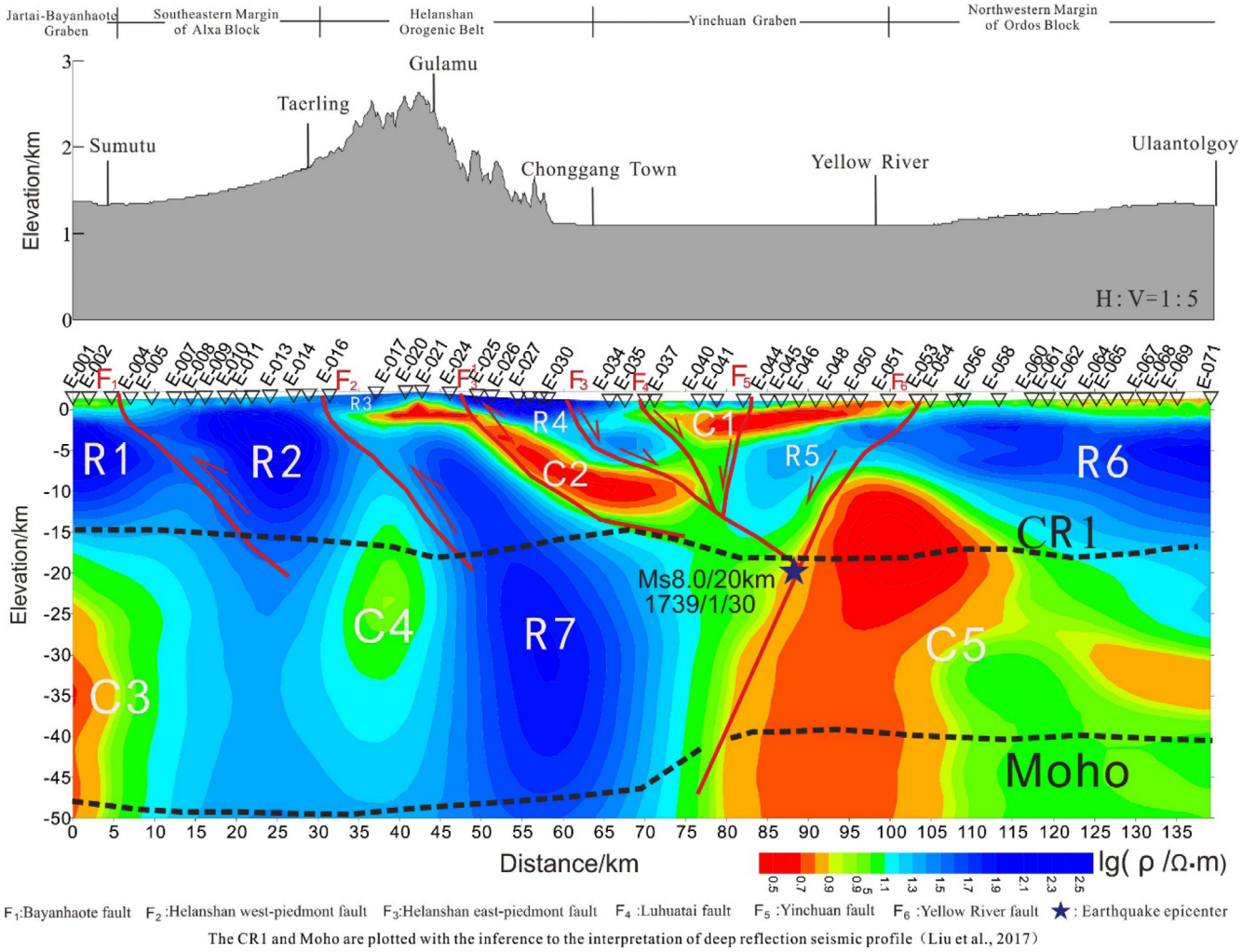

Fig. 9. A comprehensive interpretation of the deep resistivity structure along our profile E–E′. C1–C5 are conductors and R1–R6 are resistors. The site locations and local topography are also sketched on top of the model.

consistent with the characteristics of the thrust fault plane of F_2. The branch fault of F_3, named F_3^1, is interpreted as a thrust fault, dipping eastward along the highly conductor C2, based on previous geological evidence (Ningxia Bureau of Geology and Mineral Exploration and Development, 1990) and our geo-electrical model. Generally, the thrust-nappe system mentioned above has resulted in folding and uplift on the western margin of the YG.

The YG is bounded by active normal faults at both its eastern and western margins, named F_3 and F_6, respectively. F_4 and F_5 are inferred to be buried faults developed in the YG. The faults mentioned above dip towards the centre of the YG and strike NNE-SSW, which is parallel to the orientation of the YG. F_3 is the boundary fault between the HOB and YG and is inferred to be an active fault that dips southeastward to deep levels (Feng et al., 2011; Huang et al., 2013). We also observe that F_3^1 dips eastward along C2 developed beneath the HOB and intersects with F_3 at a depth of 11 km; F_3^1 is thought to be a residual trace of the eastward thrust-nappe systems of the Yinchuan faulting and uplift in the Yanshanian period (Wang et al., 2010). The F_4 and F_5 faults together have disrupted the basement of the YG, and we can see that the two blind faults dip and intersect with F_3 at depths of approximately 10 km to 15 km. F_6 is an ultra-crustal normal fault that dips westward and intersects with F_3 at a depth of approximately 20 km, and the fault plane of F_6 disrupts the basement beneath the YG and extends deeply along the resistivity gradient zone on the left side of C5. The above interpretation for F_6 is supported by seismic reflection data (Feng et al., 2011; Liu et al., 2017). Therefore, the basement structure and sedimentary thickness of the YG are controlled by negative flower-structure faults, including the HEPF, LF, YF and YRF (from west to east). Alternating activity along these faults has resulted in the present pattern of the YG and the HOB.

https://doi.org/10.1007/s12303-021-0014-6

5. ANALYSIS OF STRUCTURAL DEFORMATION

As shown in the final inversion model (Fig. 9), the deep electrical structures in different secondary tectonic belts have obvious differences.

5.1. Electrical Structure of the Upper Crust

The high-resistivity anomaly in the upper crust (above CR1) can be divided laterally into various secondary blocks, the boundaries of which are constrained by the resistivity gradient zones and are consistent with the boundary faults developed with our model. The east-dipping highly conductive body C2 revealed beneath the HOB clearly has resistivity ranges from several to dozens of Ω·m, which is consistent with previous studies of the BBMT profile across the southern YG (Wang et al., 2012). In addition, geological results have shown that many regional thrust-nappe faults of Mesozoic age have developed in the study area (Zhang et al., 2006). Therefore, we infer that C2 may be the ductile decollement zone related to thrust-nappe structures. A shallow conductor, C1, exists beneath the YG, the maximum depth of which is approximately 7 km, and a similar conductor has also been observed in the electrical model of the southern YG with a maximum depth of approximately 6 km (Wang et al., 2012). In addition, the shallow low-velocity anomalies have been revealed beneath the YG by recent studies of seismic sounding profiles, which have remarkable spatial coincidence with C1 (Liu, et al., 2017) because the depth of sedimentary strata in YG is approximately 8.0 km (Zhao et al., 2007b). Therefore, we conclude that the shallow conductive bodies beneath the YG reflect Cenozoic sedimentary strata.

The east-dipping high-resistivity bodies R1, R2, R3 and R4 revealed in the upper crust are associated in an imbricate structure, while the resistivity gradient zones caused by F_1, F_2 and F_3[1] also dip eastward to depth, and these tectonic deformation characteristics have been suggested by recent studies of P-wave receiver functions (Wang et al., 2017; Wang et al., 2018) along our profile. Considering the spatial association of the high-resistivity bodies, we infer that the upper crust on the western side of the YG shows the structural characteristics of westward thrusting. The electrical structure of the upper crust in the NWMOB is characterized by a stable block that has a layered structure. The shallow low-resistivity layers beneath the NWMOB, with a thickness of approximately 1 km, may be composed of Cenozoic sediments. The basement developed beneath the sediments has a high resistivity of hundreds of Ω·m and dips eastward to a maximum depth of approximately 30 kilometres.

Based on previous studies, we know that the high-resistivity bodies R1–R6 revealed in the upper crust may be the comprehensive response of the crystalline basement that formed in the early Palaeozoic or Proterozoic (Ningxia Bureau of Geology and Mineral Exploration and Development, 1990). Moreover, note the spatial distribution characteristics of these high-resistivity bodies in the upper crust, where the high-resistivity body R5 in the YG shows obvious depression characteristics compared with the adjacent high-resistivity bodies R4 and R6; the depression structure of the crystalline basement is controlled by the active normal faults in the YG. In addition, all the high-resistivity bodies (R1–R6) belong to the stage of a unified and stable Proterozoic to Palaeozoic massif, which has been introduced in many previous studies (Zhao et al., 2007; Liu et al., 2010; Huang et al., 2013). During the Proterozoic to Palaeozoic, the HOB was not uplifted,

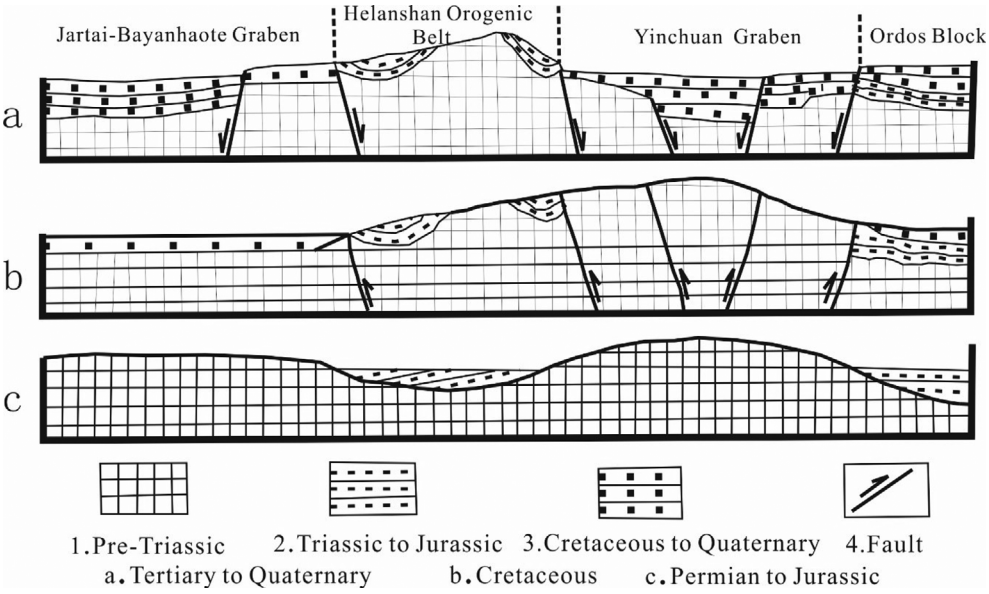

Fig. 10. The structural framework at different tectonic periods.

and the YG was not faulted. Subsequently, under the influence of Yanshanian and Himalayan tectonic movements, the present structural framework and deformation characteristics of the study area formed. Figure 10 shows structural pattern maps of the study area from the Permian to Quaternary.

5.2. Electrical Structure of the Middle–Lower Crust

Remarkable lateral inhomogeneity is revealed in the electrical structure of the middle–lower crust along our profile (under CR1), which shows alternating characteristics of high and low resistivity. The highly conductive C3, C4 and C5 developed in the middle–lower crust. The low-resistivity anomalous zone C3 developed beneath the JT-BYG, extending to great depth and crossing the Moho surface, and C4, developed beneath the HOB, dips westward. One of the most striking features of our inverse geo-electrical model is the large-scale conductive body C5 developed beneath the YG and the NWMOB; the gradient zone band on the left side of conductive body C5 is consistent with the YRF. Another feature of the resistivity model is the conductor C5 rising from the upper mantle and penetrating CR1 to the basement of the OB, for which upward arch deformation characteristics are observed beneath the eastern margin of the YG; the spatial distribution range of the conductor C5 is consistent with the in-crust conductor revealed by previous BBMT studies in the southern YG (Wang et al., 2010) and the 3D resistivity model derived from long-period magnetotelluric (LMT) data (Dong et al., 2014). As shown in Figure 9, our inverse electrical model has high resolution due to the close station spacing along profile E–E'. The conductive body C5 can be divided into two parts, and the resistivity of the left part is lower than that of the right part.

As shown in Figure 11a, the YG, HG and JT-BYG all belong to the fault basin systems of the NWMOB. The highly conductive bodies C3, C4 and C5 developed in the middle–lower crust beneath our inverse resistivity model, and previous studies show that similar highly conductive bodies are widespread beneath the fault basin systems adjacent to the northwestern OB (Qu et al., 1998; Wang et al., 2010; Dong et al., 2014; Xu et al., 2017). In addition, research results from deep seismic reflection profiles and seismic stations (Tian et al., 2011; Jiang et al., 2013; Liu et al., 2017; Wang et al., 2017; Guo et al., 2018; Wang et al., 2018) show that low-velocity anomalies are widely developed in the HG, JT-BYG and YG. The high conductors revealed by the BBMT and LMT results are coincident with the spatial distribution of low-velocity anomalies revealed by the results of seismic data studies.

The electrical structures identified in the middle and lower crust of our inverse model and the east-dipping high-resistivity anomaly R7 developed beneath the HOB, which is adjacent to the highly conductive C5 and crosses the Moho and CR1, are very remarkable relative to the resistivities on both sides, while the high-resistivity body R5 is also revealed in the geo-electrical

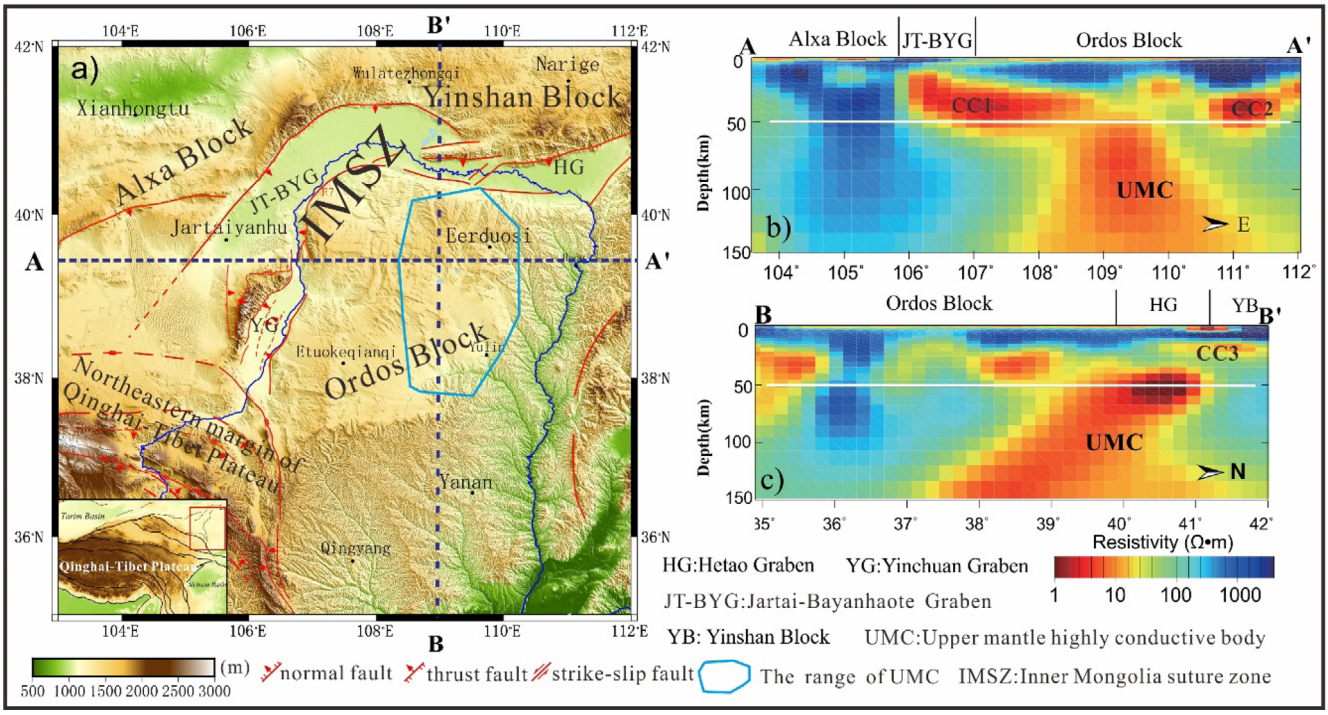

Fig. 11. Schematic illustration of dynamic processes in the study region (refer to Dong et al., 2014). The red box in the inset map shows the location of the study area. CC1 and CC2 are conductive bodies developed beneath the study area. The blue dotted line represents the position of the section A–A' and B–B'.

https://doi.org/10.1007/s12303-021-0014-6

model of a previous 2D BBMT profile across the southern YG (Wang et al., 2010). These high-conductivity and high-resistivity bodies in the YG have often been interpreted to be caused by the upwelling of mantle materials, evidence for which can be identified from the crust and the uppermost mantle electrical structures (Qu et al.,1998) and the crust and upper mantle velocity structures (Wang et al., 2018). In addition, mafic and ultramafic intrusions widely present in the southern margin of the AB (Jiao et al., 2017) indicate that upwelling of mantle materials may have occurred beneath the study area. Mantle upwelling generally causes magmatic intrusions, such as the high-resistivity body R7 revealed in our model, and may produce the weak reflection characteristics in the middle–lower crust beneath the HOB revealed by the velocity structure (Liu et al., 2017); our findings indicate that R7 may consist of Archaean or Palaeozoic granite intrusions or crystalline metamorphic rock series.

6. DYNAMIC BACKGROUND OF THE YINCHUAN GRABEN

The YG is one of the fault basins (shown in Fig. 11a) developed in the NWMOB; therefore, the evolution of these basins, including the YG, may have a similar deep dynamic background (Ningxia Bureau of Geology and Mineral Exploration and Development, 1990). To clarify the dynamic background of the fault basins, the 3D lithospheric resistivity model of the OB and adjacent areas (Dong et al., 2014) was developed based on LMT data. As shown in Figures 11b and c, two resistivity sections were derived from the final 3D model, named A–A' and B–B'. We can see that the OB is not a stable cratonic massif, and an upper-mantle highly conductive (UMC) body is revealed extending from depths of 50 km to 150 km beneath the northern part of the OB, while the blue wireframe shown in Figure 8a is the approximate projection range of the UMC on the ground. The subduction of the Palaeo-Pacific Plate caused the destruction of the North China Craton in the late Mesozoic (Griffin et al., 1998; Zhu et al., 2012); thus, the existence of the UMC may be related to the process of destruction of the NCC. In the mid-lower crust, the highly conductive CC1 and CC3 developed beneath the JT-BYG and HG dip southward and intersect with the UMC, and the spatial distribution range is consistent with the high Vp/Vs ratio zone revealed by recent studies of P-wave receiver functions (Tian et al., 2011). As shown in Figure 11a, the Inner Mongolia suture zone (IMSZ) spreads between the OB and AB (Xiao et al., 2003; Santosh, 2010; Dong et al., 2014) and may provide a channel for the upwelling of the UMC hot body and cause partial melting beneath the fault basins in the NWMOB.

In fact, the UMC and mid-lower crust highly conductive bodies developed in the NWMOB have been shown in many 2D BBMT profiles. The profile across the northern OB, HG and Yinshan Block (YB) (Xu et al., 2017) proves not only the existence of the UMC and CC3 but also the southward dip of CC3 and its intersection with the UMC. The models derived from the profile across the southern section of the YG (Wang et al., 2010) and our profile across the middle section of the YG have similar electrical structures, in which low-resistivity bodies are revealed in the mid-lower crust of the YG and intersect with the mid-lower crustal conductive body that developed beneath the OB. For the 2D and 3D geo-electrical models mentioned above, in addition to the UMC shown in Figure 9 and the mid-lower crustal conductors that developed beneath the NWMOB, the lithosphere of the AB and YG and the upper mantle in the northern part of the OB are characterized by high resistivity. Considering the spatial distribution characteristics of high-conductivity and high-resistivity bodies in the study area, we propose that the highly conductive bodies beneath the NWMOB may result from upwelling mantle material along the IMSZ that caused partial melting. When the lateral extension of the molten material was resisted by the high-resistivity bodies developed beneath the AB and YG, the molten material ascended. Based on the resistivity structures revealed by previous studies and our geo-electrical model shown in Figure 9, we propose that the massive highly conductive bodies developed in the NWMOB are related to the upwelling and lateral expansion of the UMC, which may have contributed to the formation and evolution of the fault basins in the NWMOB.

In addition, recent studies have shown that the Tibetan Plateau has been expanding to the northeast during the Cenozoic, which is related to the formation of the fault basins in the NWMOB (Cheng et al., 2014; Gao et al., 2018). Since geophysical properties can effectively reflect the deep material state of the Tibetan Plateau and adjacent areas, many seismic studies have been carried out; for example, P-wave tomography revealed continuous low-velocity asthenospheric mantle structures extending from the Tibetan Plateau to eastern China, which could have led to diffuse asthenospheric upwelling and caused the destruction of the NCC (Liu et al., 2004). The upper mantle low-velocity bodies that developed in the NWMOB have been revealed by P-wave tomography (Gao et al., 2018), consistent with the highly conductive bodies displayed by the electrical models discussed in the present paper, and the low-velocity zone extends southward to a depth of 400 kilometres below the NEMTP; thus, our findings indicate that the conductive and low-velocity zone is related to the upwelling of mantle materials originating from the NEMTP. The evidence from P-wave tomography results has also revealed obvious low-velocity anomalies at a depth of 30 km, which developed beneath the NEMTP and extend northeast along the YG-HG (Guo et al., 2018). Further, due to densely spaced seismic stations, detailed crustal and lithospheric mantle velocity structures have been

obtained, suggesting that lateral flow from the NEMTP has reached the YG between the rigid OB and AB (Shen et al., 2017). Seismic studies comparing the 3D density structure and P-wave tomography of the lithosphere in the northeastern Tibetan Plateau, in a horizontal slice at a depth of 80 km, show that on the whole, the values of density anomalies are high and the P-wave anomalies are relatively low, which may be caused by increased temperature or partial melting (Guo et al., 2004; Wang et al., 2017). Based on the above analysis, we propose that a lateral mantle flow under the northeastern Tibetan Plateau, restricted by the rigid AB and OB, extended into the gap between the two blocks, which may be the dynamic mechanism for the formation of the YG.

However, previous geological and geochemical research results indicate that the YG has undergone several major tectonic movement stages (Zhang et al., 2006; Shi et al., 2013), including initial rifting (approximately 23.8 Ma), rapid rifting (~10 Ma to ~12 Ma), continuous expansion (approximately 5.4 Ma) and re-rifting (approximately 2.6 Ma). However, the time when the Tibetan Plateau extended to the southern margin of Ningxia was ~8 Ma to ~10 Ma, and at approximately 2.7 Ma, the Tibetan Plateau extended to the SGKF, which is the surface boundary between the northeastern Tibetan Plateau and the YG (Wang et al., 2011; Wang et al., 2013). The initial rifting time of the YG is obviously not consistent with the time when the Tibetan Plateau extended to the southern margin of the YG, which indicates that the initial rifting of the YG was not related to the extension of the Tibetan Plateau. At approximately 2.6 Ma, obvious fault depressions also occurred in the YG, and at this time, the northeastern Tibetan Plateau extended to the southern YG, which indicates that the northeastward extension of the Tibetan Plateau may have caused the re-rifting of the YG. Considering the conductive and low-velocity bodies developed beneath the NWMOB, their relationship with the UMC developed beneath the northern OB, and the contact relationship with the northeastern Tibetan Plateau, we conclude that the formation and evolution of the YG may have been controlled by various dynamic mechanisms.

From the late Palaeozoic to the early Tertiary, the YG and surrounding areas were uplifted as a whole, and sedimentary records of this period are lacking (The Research Group on Active Fault System around Ordos Massif of the National Seismological Bureau of China, 1988).

In the late Jurassic, affected by the Yanshanian movement, NNE-trending thrust faults developed along the YG to HG (Deng et al., 1999). According to the spatial distribution of highly conductive bodies in the NWMOB and considering the results of previous isotopic geochronologic studies, the initial rifting of the YG in the period from the Eocene to the Oligocene can be interpreted by the schematic cartoon shown in Figure 12a. Upwelling material beneath the northern OB started to rise from the upper mantle and was blocked by the rigid lithosphere mantle of the AB; thus, the upwelling mantle material continued rising along the south-dipping suture zone between the AB and the OB, which could have extended laterally to the lower crust and induced the highly conductive bodies beneath the NWMOB. Alternatively, because of the upwelling mantle material, a tensional tectonic environment was formed, and rifting and uplifting along large thrust faults developed during the Yanshanian period, which formed the initial framework of the YG and the HOB.

As mentioned above, in the late Pliocene (approximately 3 Ma), the northeastern Tibetan Plateau had extended to the southern margin of the YG, while re-rifting occurred in the YG at almost the same time. Considering the crust-mantle structures of the northeastern Tibetan Plateau revealed by previous research and our geophysical data, we propose that the evolution of the YG after the late Pliocene may also have been affected by the NE-trending expansion of the Tibetan Plateau, which can be described by the schematic cartoon shown in Figure 12b. Further, as we noted, the low-velocity and high-conductivity bodies that developed beneath the northeastern Tibetan Plateau between the upper and lower crust, named the middle crustal decollement layers, have been revealed by previous geophysics results (Min et al., 2012; Li et al., 2014; Liu et al., 2014; Wang et al., 2014; Zhang et al., 2015). As shown in Figure 12b, lateral material flow of the lower crust and upper mantle in the NEMTP, constrained by the middle crustal decollement layers and asthenospheric mantle, extended northeastward to the gap between the OB and AB and was blocked by the rigid lithosphere mantle of these basins, which directed the lateral material flow upward and has affected the evolution of the YG since the end of the Pliocene. The dynamic model shown in Figure 12b is similar to the model used to explain the uplift and eastward expansion of the Tibetan Plateau (Wang et al., 2015; Teng et al., 2018) and has been used to research the dynamic mechanism of the Wenchuan earthquake on the eastern margin of the Tibetan Plateau.

7. SEISMOGENIC STRUCTURE OF THE PINGLUO EARTHQUAKE

The Pingluo Ms8.0 earthquake in 1739 occurred in the YG. Previous studies on seismogenic structures of the Pingluo earthquake in the YG are still controversial; for example, some researchers assert that the buried YF was the causative fault (Li et al., 1984), whereas other researchers consider the HEPF to be the causative fault (Ding et al., 1993; Lei et al., 2015), and still scholars have proposed that synchronous activity along the YF and HEPF resulted in the occurrence of the Pingluo earthquake

https://doi.org/10.1007/s12303-021-0014-6

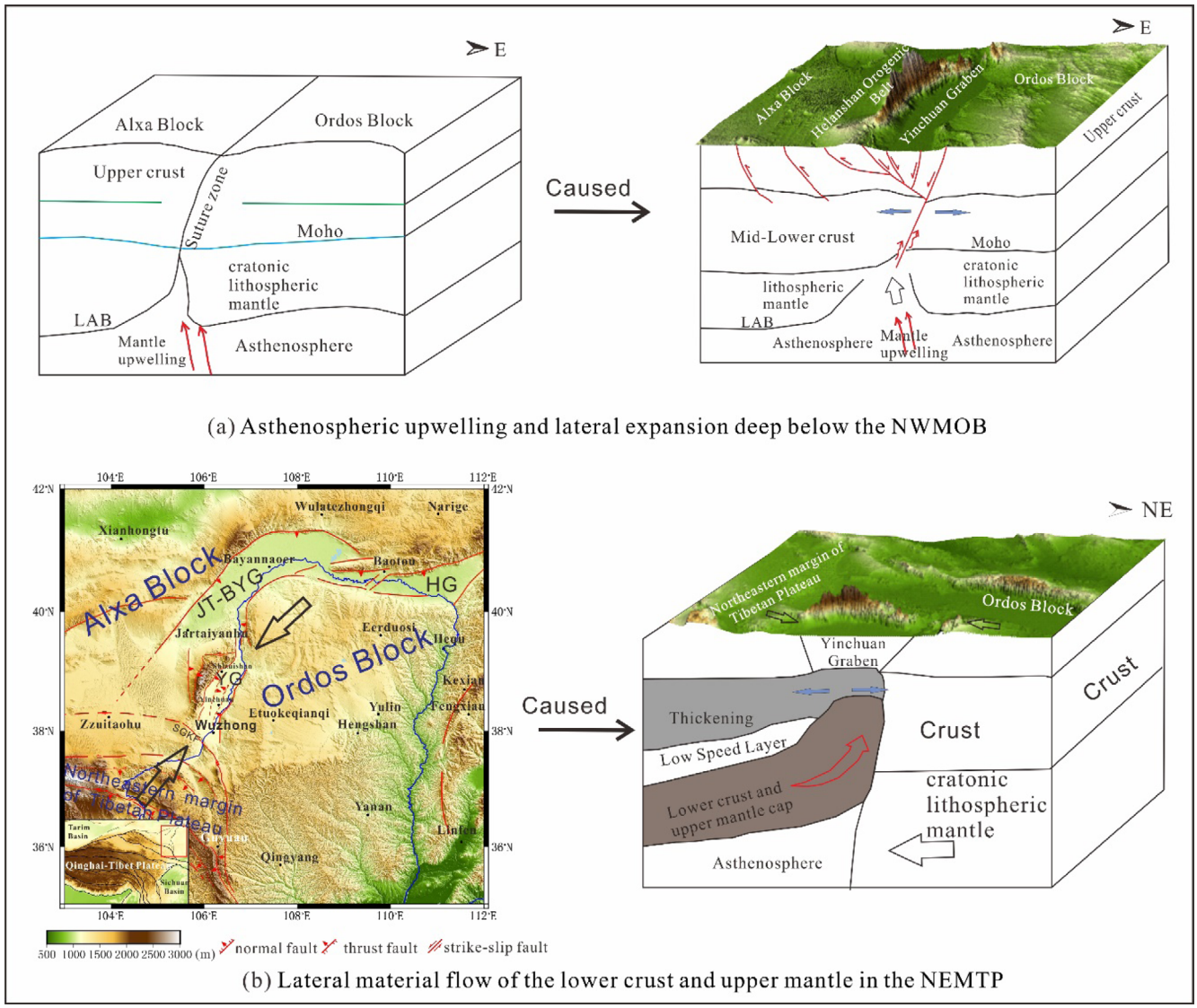

Fig. 12. Deep dynamic mechanism for the formation and evolution of the YG. The open arrows show the movement of tectonic units, while the closed arrows show predicted surface motion. LAB: The Boundary between lithosphere and asthenosphere, NWMOB: Northwestern margin of the Ordos Block, NEMTP: Northeastern margin of the Tibetan Plateau.

(Chai et al., 2011). In this paper, as shown in Figure 9, the epicentral projection point of the Pingluo earthquake is located at the intersection of the HEPF and YRF, which is consistent with the epicentre revealed by seismic structures (Feng et al., 2011) and with our location for the seismogenic structure of the Pingluo Ms8.0 earthquake in 1739. Considering the epicentre revealed by the electrical structure and seismic structure, the YRF or the HEPF was more likely to have been the causative fault of the Pingluo earthquake, which may also have been controlled by both faults. As mentioned above, the YG and adjacent areas have undergone strong intercontinental tectonic deformation due to mantle upwelling, uplift and extension of the NEMTP and blocking by the rigid AB and OB. Previous studies have proven that medium-strength earthquakes are mostly located in transitional zones separating high-resistivity from low-resistivity areas (Wang et al., 2014; Zhan et al., 2017; Xia et al., 2018). Remarkably, adjacent high- and low-resistivity bodies have also been revealed in our electrical structure crossing the YG. Against this tectonic background, tectonic stress easily accumulates beneath the YG and induces the occurrence of moderate-strength earthquakes. Based on the analysis in this paper, we indicate that the high-conductivity and low-velocity body C5 has continued pushing upward with the upwelling mantle material during the Cenozoic under a tensional tectonic environment along the boundary faults (the YRF and HEPF) of the YG. The tectonic stress shifted into the intersection (at a depth of approximately 20 km) between the two faults, and when the stress concentration reached the critical state, the Pingluo earthquake occurred.

8. CONCLUSIONS

In this paper, based on our preferred resistivity model obtained using the 2D inversion method, and combining deep geological and geophysical research results from the NWMOB and NEMTP, we discuss the deep dynamic background for the evolution of YG, and the main conclusions are as follows:

(1) A dramatic lateral resistivity contrast from the AB to the OB is revealed by our model. In the YG and adjacent areas, the deformation of the upper crust is different from that of the lower crust. The high-resistivity body developed in the basement of the YG shows obvious depression characteristics relative to the AB to the west and the OB to the east. High-resistivity and low-resistivity bodies developed alternately in the lower crust; the high-resistivity body in the lower crust beneath the HOB may be caused by an intrusive rock mass, and highly conductive and low-velocity bodies in the lower crust beneath the YG may be caused by upwelling mantle materials.

(2) The formation and evolution of the YG are related to upwelling mantle materials, which may be controlled by various dynamic mechanisms. From the Eocene to Oligocene, highly conductive hot mantle materials or melts beneath the northern OB extended northwestward along the IMSZ, were blocked by the rigid AB and caused the formation of the YG. Further, from the late Pliocene to the present, in addition to upwelling mantle materials beneath the northern OB, the NE-trending expansion of the Tibetan Plateau may have affected the evolution of the YG.

(3) Based on the electrical and velocity models, we indicate that the deep intersection between the YRF and HEPF, at a depth of approximately 20 km, was the preferred seismogenic structure of the 1739 Pingluo earthquake, which occurred in the northern part of the North-South Seismic Belt in China and was related to the NE-trending expansion of the Tibetan Plateau, the upwelling of mantle materials, and the continuous movements along the boundary faults of the YG.

ACKNOWLEDGMENTS

We thank the Ningxia Bureau of Geology and Mineral Exploration and Development of China for providing help with BBMT data acquisition. We are grateful for Dr. Hao Dong for providing previous MT data in the study area. This work is supported by the National Natural Science Foundation of China (Grants 91755215, 41330212) and the China Geological Survey (DD20190033). Several figures were created with Generic Mapping Tools (Wessel and Smith, 1998).

REFERENCES

Bai, D.H., Unsworth, M.J., and Meju, M.A., 2010, Crustal deformation of the eastern Tibetan plateau revealed by magnetotelluric imaging. Nature Geoscience, 3, 358–362.

Becken, M., Ritter, O., Bedrosian, P.A., and Weckmann, U., 2011, Correlation between deep fluids, tremor and creep along the central San Andress fault. Nature, 480, 87–90.

Cai, J.T. and Chen X.B., 2010, Refined techniques for data processing and two-dimensional inversion in magnetotelluric II: Which data polarization mode should be used in 2D inversion. Chinese Journal of Geophysics, 53, 2703–2714. (in Chinese with English abstract)

Cai, J.T., Chen, X.B., and Zhao, G.Z., 2010, Refined techniques for data processing and two-dimensional inversion in magnetotelluric I: Tensor decomposition and dimensionality analysis. Chinese Journal of Geophysics, 53, 2516–2526. (in Chinese with English abstract)

Caldwell, T.G., Bibby, H.M., and Brown, C., 2004, The magnetotelluric phase tensor. Geophysics Journal International, 158, 457–469. (in Chinese with English abstract)

Chai, C.Z., Meng, G.K., and Ma, G.R., 2011, General situation of regional seismogeology. In: Xu, X.W. (ed.), Active Fault Detection and Seismic Hazard Assessment in Yinchuan City. Science Press, Beijing, p. 17–53. (in Chinese)

Chave, A.D. and Jones, A.G., 2012, The Magnetotelluric Method: Theory and Practice. Cambridge University Press, Cambridge, 552 p.

Deng, Q.D., Cheng, S.P., Min, W., Yang, G.Z., and Ren, D.W., 1999, Discussion on Cenozoic tectonics and dynamics of Ordos Block. Journal of Geomechanics, 5, 12–21.

Ding, G.Y., Tian, Q.J., Kong, F.C., Xie, X., Zhang, L., and Wang, L., 1993, Segmentation of Active Faults: Principles, Methods and Applications. Seismological Press, Beijing, 143 p. (in Chinese)

Dong, H., Wei, W.B., Ye, G.F., Jin, S., Jones, A.G., Jing, J.E., Zhang, L.T., Xie, C.L., Zhang, F., and Wang, H., 2014, Three-dimensional electrical structure of the crust and upper mantle in Ordos Block and adjacent area: evidence of regional lithospheric modification. Geochemistry Geophysics Geosystems, 15, 2414–2425.

Egbert, G.D. and Booker, J.R., 1986, Robust estimation of geomagnetic transfer functions. Geophysical Journal International, 87, 173–194.

Feng, S.Y., Gao, R., Long, C.X., Fang, S.M., Zhao, C.B., Kou, K.P., Tan, Y.L., and He, H.Y., 2011, The compressive stress field of Yinchuan Graben: deep seismic reflection profile. Chinese Journal of Geophysics, 54, 692–697. (in Chinese with English abstract)

Gao, X., Guo, B., Chen, J.H., Liu, Q.Y., Li, S.C., and Li, Y., 2018, Rebuilding of the lithosphere beneath the western margin of Ordos: evidence from multiscale seismic tomography. Chinese Journal of Geophysics, 61, 2736–2749. (in Chinese with English abstract)

Griffin, W.L., Zhang, A.D., O'Reilly, S.Y., and Ryan, C., 1998, Phanerozoic evolution of the lithosphere beneath the Sino-Korean Craton. In: Flower, M.F.J., Chung, S.-L., Lo, C.-H., and Lee, T.-Y. (eds.), Mantle Dynamics and Plate Interactions in East Asia. AGU Geodynamic Series, American Geophysical Union, Washington, D.C., 27, p. 107–126.

Guo, H.L. and Ding, Z.F., 2018, Crustal velocity structure beneath the northern North-South seismic zone from local seismic tomography and its tectonic implications. Acta Seismologica Sinica, 40, 547–562. (in Chinese with English abstract)

https://doi.org/10.1007/s12303-021-0014-6

Guo, B., Liu, Q.Y., Chen, J.H., Zhao, D.P., Li, S.C., and Lai, Y.G., 2004, Seismic tomographic imaging of the crust and upper mantle beneath the Northeastern edge of the Qinghai-Xizang plateau and the Ordos area. Chinese Journal of Geophysics, 47, 790–797. (in Chinese with English abstract)

Huang, X.F., Shi, W., Li, H.Q., Chen, L., and Cen, M., 2013, Cenozoic tectonic evolution of the Yinchuan Basin: constraints from the deformation of its boundary faults. Earth Science Frontiers, 20, 199–210. (in Chinese with English abstract)

Jiang, M.M., Ai, Y.S., Chen, L., and Yang, Y.J., 2013, Local modification of the lithosphere beneath the central and western North China Craton: 3D constraints from Rayleigh wave tomography. Gondwana Research, 24, 849–864.

Jiao, J.G., Ma, Z.M., Lu, H., Gao, D., Zhang, G.P., and Shao, L.Q., 2017, Zircon U-Pb dating of Yejili mafic-ultramafic intrusions in the southern margin of the Alax block and their geological significance. Geotectonica et Metallogenia, 41, 950–959. (in Chinese with English abstract)

Jin, J.M. and Wang, J.G., 1998, Finite Element Method of Electromagnetic Field. Xi'an University of Electronic Science and Technology Press, Xi'an, 96 p. (in Chinese with English abstract)

Ledo, J., Queralt, P., Marti, A., and Jones, A.G., 2002, Two-dimensional interpretation of three dimensional magnetotelluric data: an example of limitations and resolution. Geophysical Journal International, 150, 127–139.

Lei, Q.Y., Cai, C.Z., Du, P., Yu, J.X., Wang, Y., and Xie, X.F., 2015, The seismogenic structure of the Ms8.0 Pingluo earthquake in 1739. Seismology and Geology, 37, 413–429. (in Chinese with English abstract)

Lei, Q.Y., Zhang, P.Z., Zheng, W.J., Chai, C.Z., Wang, W.T., Du, F., and Yu, J.X., 2016, Dextral strike-slip of Sanguankou-Niushoushan fault zone and extension of arc tectonic belt in the northeastern margin of the Tibet Plateau. Science China Earth Sciences, 59, 1025–1040.

Lei, Q.Y., Zhang, P.Z., Zheng, W.J., Du, P., Wang, W.T., Yu, J.X., and Xie, X.F., 2017, Geological and geomorphic evidence for dextral strike slip of the HelanShan west-piedmont fault and its tectonic implications. Seismology and Geology, 39, 1297–1315.

Li, M. and Gao, J.M., 2010, Basement faults and volcanic rock distributions in the Ordos Basin. Science China Earth Sciences, 53, 1625–1633.

Li, Y.K., Gao, R., Mi, S.X., Yao, Y.T., Gao, J.W., Li, W.H., and Xiong, X.S., 2014, The characteristics of crustal velocity structure for Liupan Mountain-Orsos Basin in the northeastern margin of Qinghai-Xizang (Tibet) Plateau. Geological Review, 60, 1147–1157.

Li, Q.H., Guo, S., and Lü, D.H., 1999, The Deep Structures and Tectonics of Western and Southwestern Margins of Ordos Block. Seismological Press, Beijing, 246 p. (in Chinese)

Li, M.L. and Wan, Z.C., 1984, Characteristics of the earthquake-generating structures for magnitude 8.0 Pingluo earthquake of 1739 and the process of its preparation. Seismology and Geology, 6, 23–28. (in Chinese with English abstract)

Lin, J.Y., Liu, B.J., Zhang, Z.K., and Duan, Y.H., 2017, Lithosphere structure of Yinchuan basin from a long-range seismic wide angle reflection and refraction profile. Acta Seismologica Sinica, 39, 669–681. (in Chinese with English abstract)

Liu, M., Cui, X.J., and Liu, F.T., 2004, Cenozoic rifting and volcanism in eastern China: a mantle dynamic link to the Indo-Asian collision. Tectonophysics, 393, 29–41.

Liu, B.J., Feng, S.Y., Ji, J.F., Wang, S.J., Yuan, H.K., and Yang, G.J., 2017, Lithospheric structure and faulting characteristics of the Helan Mountains and Yinchuan Basin: results of deep seismic reflection profiling. Science China Earth Sciences, 60, 589–601.

Liu, J.H., Zhang, P.Z., Zheng, D.W., Wan, J.L., Wang, W.T., Du, P., and Lei, Q.Y., 2010, Pattern and timing of late Cenozoic rapid exhumation and uplift of the Helan Mountain, China. Science China Earth Sciences, 53, 345–355.

Liu, Q.M., Zhao, J.M., Lu, F., and Liu, H.B., 2014, Crustal structure of northeastern margin of the Tibetan Plateau by receiver function inversion. Science China Earth Sciences, 57, 741–750.

Menzies, M.A., Fan, W.M., and Zhang, M., 1993, Palaeozoic and Cenozoic lithoprobes and the loss of > 120 km of Archaean lithosphere, Sino-Korean craton, China. In: Pritchard, H.M., Alabaster, T., Harris, N.B.W., and Neary, C.R. (eds.), Magmatic Processes and Plate Tectonics. Geological Society, London, Special Publications, 76, p. 71–81.

Mohan, L., Rastogi, B.K., and Chaudhary, P., 2015, Magnetotelluric studies in the epicenter zone of 2001, Bhuj earthquake. Journal of Asian Earth Sciences, 98, 75–84.

Murphy, B.S. and Egbert, G.D., 2017, Electrical conductivity structure of southeastern North America: implications for lithospheric architecture and Appalachian topographic rejuvenation. Earth and Planetary Science Letters, 462, 66–75.

Ningxia Bureau of Geology and Mineral Exploration and Development, 1990, Regional Geological Records of Ningxia in China. Geological Press, Beijing, 392 p. https://max.book118.com/html/2019/0207/7115012110002005.shtm [Accessed on 12 April 2021] (in Chinese)

Qu, J.P., 1998, The relation between the deep-electrical structure of the west and southwest margin of Ordos Block and the geological structure in this area. Inland earthquake, 12, 313–319. (in Chinese with English abstract)

Rodi, W. and Mackie, R.L., 2001, Nonlinear conjugate gradients algorithm for 2D magnetotelluric inversion. Geophysics, 66, 174–187.

Santosh, M., 2010, Assembling North China Craton within the Columbia supercontinent: the role of double-sided subduction. Precambrian Research, 178, 149–167.

Shao, Z.G. and Zhang, L.P., 2013, Study of strong earthquake recent trends on the northern segment of North-South seismic belt. Earthquake Research in China, 29, 26–36. (in Chinese with English abstract)

Shen, X.Z., Liu, M., Gao, Y., Wang, W.J., Shi, Y.T., An, M.J., Zhang, Y.S., and Liu, X.Z., 2017, Lithospheric structure across the northeastern margin of the Tibetan Plateau: implications for the plateau's growth. Earth and Planetary Science Letters, 459, 80–92.

Shi, W., Liu, Y., Liu, Y., Chen, P., Chen, L., Cen, M., Huang, X.F., and Li, H.Q., 2013, Cenozoic evolution of the Haiyuan fault zone in the northeast margin of the Tibetan Plateau. Earth Science Frontiers, 20, 1–17. (in Chinese with English abstract)

Teng, J.W., Song, P.H., and Liu, Y.S., 2018, Geophysical background field and deep dynamics of the Wenchuan-Yingxiu Ms8.0 earthquake. Chinese Science Bullutin, 63, 1882–1905. (in Chinese with English

abstract)

The Research Group on Active Fault System around Ordos Massif of the National Seismological Bureau of China, 1988, Active Fault System around Ordos Massif. In Jiang, H.X. and Li, H.J. (eds.), Characteristics of Quaternary Movement of Yinchuan-Jartai Down-faulted Basin Belt. Seismological Press, Beijing, p. 20–27. (in Chinese)

Tian, Z.Y., Han, P., and Xu, K.D., 1992, The Mesozoic–Cenozoic East China rift system. Tectonophysics, 208, 341–363.

Tian, X.B., Teng, J.W., Zhang, H.S., Zhang, Y.Q., Yang, H., 2011, Structure of crust and upper mantle beneath the Ordos Block and the Yinshan Mountains revealed by receiver function analysis. Physics of the Earth Planetary Interiors, 184, 186–193.

Unsworth, M., Wei, W.B., Jones, A.G., Li, S.H., Bedrosian, P., Booker, J., Sheng, J., Deng, M., and Tan, H.D., 2004, Crustal and upper mantle structure of northern Tibet imaged with magnetotelluric data. Journal of Geophysical Research, 109, B02403.

Wang, W.T., 2011, Sedimentary responses to the Cenozoic tectonic evolution of the northeastern corner of the Tibetan Plateau. The Institute of Geology, China Seismological Bureau, Beijing, 66 p. (in Chinese with English abstract)

Wang, W.T., Kirby, E., Zhang, P.Z., and Zheng, D.W., 2013, Tertiary basin evolution along the northeastern margin of the Tibetan plateau: Evidence for basin formation during Oligocene transtension. Geological Society of America Bulletin, 125, 377–400.

Wang, X.S., Fang, J., and Xu, H.Z., 2013, 3D density structure of lithosphere beneath northeastern margin of the Tibetan Plateau. Chinese Journal of Geophysics, 56, 3770–3778. (in Chinese with English abstract)

Wang, H.Y., Gao, R., Li, Q.S., Li, W.H., Hou, H.S., Kuang, C.Y., Xue, A.M., and Huang, W.Y., 2014, Deep seismic reflection profiling in the Songpan-west Qingling-Linxia basin of the Qinghai-Tibet plateau: data acquisition, data processing and preliminary interpretation. Chinese Journal of Geophysics, 57, 1451–1461. (in Chinese with English abstract)

Wang, S.J., Liu, B.J., Jia, S.X., Deng, X.G., Song, X.H., and Li, Y.Q., 2017, Study on S-wave velocity structure difference of Yinchuan basin and blocks on both sides using artificial seismic sounding profiles. Progress in Geophysics, 32, 1936–1943. (in Chinese with English abstract)

Wang, S.J., Liu, B.J., Tian, X.F., Liu, B.F., Song, X.H., Deng, X.G., Sun, Y.A., Ma, C.J., and Yang, Y.D., 2018, Crustal P-wave velocity structure in the northeastern margin of the Qinghai-Tibetan Plateau and insights into crustal deformation. Science China Earth Sciences, 61, 1221–1237.

Wang, Z., Su, J.R., Liu, C.X., and Cai, X.L., 2015, New insights into the generation of the 2013 Lushan earthquake (Ms 7.0), China. Journal of Geophysical Reseach: Solid Earth, 120, 3507–3526.

Wang, C.Y., Yang, W.C., Wu, J.P., and Ding, Z.F., 2015, Study on the lithospheric structure and earthquakes in North-South tectonic belt. Chinese Journal of Geophysics, 58, 3867–3901. (in Chinese with English abstract)

Wang, X., Zhan, Y., Zhao, G.Z., Wang, L.F., and Wang, J.J., 2010, Deep electric structure beneath the northern section of the western margin of the Ordos basin. Chinese Journal of Geophysics, 53, 595–604. (in Chinese with English abstract)

Wang, X.B., Zhang, G., Fang, H., Luo, W., Zhong, Q., Cai, X.L., and Luo, H.Z., 2014, Crust and upper mantle resistivity structure at middle section of Longmenshan, eastern Tibetan plateau. Tectonophysics, 619, 143–148.

Wannamaker, P.E., Jiracek, G.R., Stodt, J.A., and Caldwell, T., 2002, Fluid generation and pathways beneath an active compressional orogen, the New Zealand Southern Alps, inferred from magnetotelluric data. Journal of Geophysical Research: Solid Earth, 107, ETG 6-1–ETG 6-20.

Wei, W.B., Unsworth, M.J., and Jones, A.G., 2001, Detection of widespread fluids in the Tibetan crust by magnetotelluric studies. Science, 292, 716–719.

Wessel, P. and Smith, W.H.F., 1998, New, improved version of generic mapping tools released. Eos, 79, 579.

Wu, F.Y., Xu, Y.G., Gao, S., and Zheng, J.P., 1988, Lithospheric thinning and destruction of the North China Craton. Acta Petrologica Sinica, 24, 1145–1174. (in Chinese with English abstract)

Xia, S.B., Wang, X.B., Min, G., Hu, Y.B., Li, D.W., Kong, F.T., and Cai, X.L., 2019, Crust and uppermost mantle electrical structure beneath Qilianshan Orogenic Belt and Alax block in northeastern margin of Tibetan Plateau. Chinese Journal of Geophysics, 62, 950–966. (in Chinese with English abstract)

Xiao, W.J., Windley, B.F., Hao, J., and Zhai, M.G., 2003, Accretion leading to collision and the Permian Solonker suture, Inner Mongolia, China: termination of the central Asian orogenic belt. Tectonics, 22, 1069.

Xu, L.B., Wei, W.B., Jin, S., Ye, G.F., Liang, H.D., Jia, C.X., Gong, X., and Yu, Y., 2017, Study of deep electrical structure along a profile from northern Ordos block to Yinshan orogenic belt. Chinese Journal of Geophysics, 60, 575–584. (in Chinese with English abstract)

Xu, T., Zhang, M.H., Tian, X.B., Zheng, Y., Bai, Z.M., Wu, C.L., Zhang, Z.J., and Teng, J.W., 2014, Upper crustal velocity of Lijiang–Qingzhen profile and its relationship with the seismogetic environment of the Ms6.5 Ludian earthquake. Chinese Journal of Geophysics, 57, 3069–3079. (in Chinese with English abstract)

Yin, B.X., Cheng, J.H., Min, G., Cai, X.L., and Yang, Y., 2013, The conductivity characteristics of middle and upper crust of Jingyuan-Yanchi, Southern Ningxia arc structure. Earth Science Frontiers, 20, 332–339. (in Chinese with English abstract)

Zhan, Y., Yang, H., Zhao, G.Z., Zhao, L.Q., and Sun, X.Y., 2017, Deep electrical structure of crust beneath the Madongshan step area at the Haiyuan fault in the northeastern margin of the Tibetan plateau and tectonic implications. Chinese Journal of Geophysics, 60, 2371–2384. (in Chinese with English abstract)

Zhan, Y., Zhao, G.Z., Wang, L.F., Wang, J.J., Chen, X.B., Zhao, L.Q., and Xiao, Q.B., 2014, Deep electric structure beneath the intersection area of West Qinling orogenic zone with North-South seismic tectonic zone in China. Chinese Journal of Geophysics, 57, 2594 –2607. (in Chinese with English abstract)

Zhang, P.Z., Deng, Q.D., Zhang, G.M., Ma, J., Gan, W.J., Min, W., Mao, F.Y., and Wang, Q., 2003, Active tectonic blocks and strong earthquakes in the continent of China. Science China Earth Sciences, 46, 13–24. https://doi.org/10.1360/03dz0002

Zhang, H.S., Gao, R., Tian, X.B., Teng, J.W., Li, Q.S., Ye, Z., Liu, Z., and Si, S.K., 2015, Crustal S wave velocity beneath the northeastern

Tibetan plateau inferred from teleseismic P wave receiver functions. Chinese Journal of Geophysics, 58, 3982–3992. (in Chinese with English abstract)

Zhang, Y.Q., Liao, C.Z., Shi, W., and Hu, B., 2006, Neotectonic evolution of the peripheral zones of the Ordos basin and geodynamic setting. Geological Journal of China Universities, 12, 285–297. (in Chinese with English abstract)

Zhang, Y.Q., Mercier, J.L., and Vergely, P., 1998, Extension in the graben systems around the Ordos (China), and its contribution to the extrusion tectonics of south China with respect to Cobi-Mongolia. Tectonophysics, 285, 41–75.

Zhang, Y.Q., Shi, W., Liao, C.Z., and Hu, B., 2006, Fault kinematic analysis and change in late Mesozoic stress regimes in the peripheral zones of the Ordos basin, north China. Acta Geologica Sinica, 80, 639–647. (in Chinese with English abstract)

Zhang, Y.Q., Vergely, P., and Mercier, J.L., 1999, Pliocene–Quaternary faulting pattern and left-slip propagation tectonics in North China. Episodes, 22, 84–88.

Zhao, L., Allen, R.M., Zheng, T.Y., and Zhu, R.X., 2012, High-resolution body wave tomography models of the upper mantle beneath eastern China and the adjacent areas. Geochemistry Geophysics Geosystems, 13, 1–20.

Zhao, C.B., Fang, S.M., Liu, B.J., Ji, J.F., Feng, S.Y., Guo, X.J., Li, J.C., and Qing, X.Y., 2009, Experiment on fault tectonics with deep seismic reflection detection in Yinchuan Basin. Journal Geodesy and Geodynamics, 29, 33–38. (in Chinese with English abstract)

Zhao, H.G., Liu, C.Y., Wang, F., Wang, J.Q., Li, Q., and Yao, Y.M., 2007, Uplift and evolution of Helan Mountain. Science China Earth Sciences, 50, 217–226. https://doi.org/10.1007/s11430-007-6010-5

Zhao, G.Z., Unsworth, M.J., Zhan, Y., and Wang, L.F., 2014, Crustal structure and rheology of the Longmenshan and Wenchuan Mw7.9 earthquake epicentral area from magnetotelluric data. Geology, 40, 1139–1142.

Zhao, D.P., Wang, Z., Umino, N., and Hasegawa, A., 2007a, Tomographic imaging outside a seismic network: application to the northeast Japan arc. Bulletin of the Seismological Society of America, 97, 1121–1132.

Zheng, J.P., O'Reilly, S.Y., and Griffin, W., 2001, Relict refractory mantle beneath the eastern North China Block: significance for lithosphere evolution. Lithos, 57, 43–66.

Zhu, R.X., Xu, Y.G., Zhu, G., Zhang, H.Q., Xia, Q.K., and Zheng, T.Y., 2012, Destruction of the North China Craton. Science China Earth Sciences, 55, 1565–1587.